Statistica Sinica Preprint No: SS-2023-0071	
Title	Statistical Inference for Mean Functions of Complex 3D Objects
Manuscript ID	SS-2023-0071
URL	http://www.stat.sinica.edu.tw/statistica/
DOI	10.5705/ss.202023.0071
Complete List of Authors	Yueying Wang, Guannan Wang, Brandon Klinedinst, Auriel Willette and Lily Wang
Corresponding Authors	Lily Wang
E-mails	lwang41@gmu.edu
Notice: Accepted version subject to English editing.	

STATISTICAL INFERENCE FOR MEAN FUNCTIONS OF COMPLEX 3D OBJECTS

Yueying Wang[1], Guannan Wang[2], Brandon Klinedinst[3]
Auriel Willette[4], and Li Wang[5]

[1]*Amazon.com, Inc., Bellevue, WA 98170, USA.*
[2]*William & Mary, Williamsburg, VA 23185, USA.*
[3]*University of Washington, Seattle, WA 98195, USA.*
[4]*Iowa State University, Ames, IA 50011, USA.*
[5]*George Mason University, Fairfax, VA 22030, USA.*

Abstract: The use of complex three-dimensional (3D) objects is growing in various applications as data collection techniques continue to evolve. Identifying and locating significant effects within these objects is essential for making informed decisions based on the data. This article presents an advanced nonparametric method for learning and inferring complex 3D objects, enabling accurate estimation of the underlying signals and efficient detection and localization of significant effects. The proposed method addresses the problem of analyzing irregular-shaped 3D objects by modeling them as functional data and utilizing trivariate spline smoothing based on triangulations to estimate the underlying signals. We develop a highly efficient procedure that accurately estimates the mean and covariance functions, as well as the eigenvalues and eigenfunctions. Furthermore, we rigorously establish the asymptotic properties of these estimators. Additionally, a novel approach for constructing simultaneous confidence corridors to quantify estimation uncertainty is presented, and the procedure is extended to accommodate comparisons between two independent samples. The finite-sample performance of the proposed methods is illustrated through numerical experiments and a real-data application using the Alzheimer's Disease Neuroimaging Initiative database.

Key words and phrases: Complex object analysis; Functional principal component analysis; Localization; Simultaneous confidence corridors; Triangulation; Trivariate splines.

1. Introduction

As data collection techniques continue to advance, complex three-dimensional (3D) objects are becoming more prevalent in new statistical applications. To effectively extract information from these objects, it is often necessary to utilize multiple images captured from different perspectives. These 3D images play a critical role in areas such as biomedical research, robotics, and engineering. For example, in medical imaging, 3D images are used to create detailed human body scans, such as magnetic resonance imaging (MRI), functional MRI, and positron emission tomography (PET) imaging. All these images can be used to diagnose and treat a variety of medical conditions. When working with complex objects, one essential task is to identify and locate significant effects. Localization, the process of identifying specific regions within the object where the signal is strong or where differences exist between different groups of subjects, plays a crucial role in making inferences about the underlying object or phenomenon. In medical imaging, for instance, localization can be used to identify specific regions of the brain or body that are associated with certain diseases or conditions.

In data analysis problems involving complex objects, the typical data structure often consists of the repeated observation and alignment of functional observations or images on a fine grid. This type of data exhibits several distinctive characteristics that pose a number of challenges (Zhu et al., 2022). For example, a degree of spatial correlation is almost universally presented (Scouten et al., 2006; Bowman et al., 2008), and failure to take into account both spatial correlation and smoothness in statistical analysis can result in significant inaccuracies in both prediction and estimation, reducing the overall statistical power (Zhu et al., 2014). Functional data analysis (FDA) offers advanced tools to effectively analyze and understand these complex data structures

(Wang et al., 2016). In this article, we present a functional regression framework that incorporates FDA techniques and considers the 3D functional information of a complex object as the response variable in the analysis. This approach is different from traditional multivariate data analysis as FDA considers the continuity of the underlying function and models the data in the functional space rather than treating them as a set of vectors (Ramsay and Silverman, 2005).

Specifically, we consider the observed data objects as realizations of a continuous stochastic process $Y(\boldsymbol{z})$, where $\boldsymbol{z} = (z_1, z_2, z_3) \in \Omega$ is a 3D coordinate in a bounded domain $\Omega \subset \mathbb{R}^3$, and $Y(\boldsymbol{z})$ represents the real-valued outcome of interest. We have n randomly selected objects, each with a corresponding functional observation $Y_i(\boldsymbol{z})$, which are considered to be independent copies of the process $Y(\boldsymbol{z})$. It is common for data on complex objects to contain noise, for example, due to limitations in data collection techniques. To account for individual variations and measurement errors in our analysis, we propose the following general functional object response regression model: for any $\boldsymbol{z} \in \Omega$,

$$Y_i(\boldsymbol{z}) = \mu(\boldsymbol{z}) + \eta_i(\boldsymbol{z}) + \sigma(\boldsymbol{z})\varepsilon_i(\boldsymbol{z}), \ i = 1, \ldots, n, \tag{1.1}$$

where $\mu(\boldsymbol{z})$ is the mean function, $\eta_i(\boldsymbol{z})$ is the random process representing the functional random effect of object i, $\sigma(\boldsymbol{z}) > 0$ is a deterministic function, and $\varepsilon(\boldsymbol{z})$ is a white noise measurement error with mean zero and variance one. We assume that $\eta_i(\boldsymbol{z})$ and $\varepsilon_i(\boldsymbol{z})$ are mutually independent, and $\eta_i(\boldsymbol{z})$ are i.i.d. copies of a stochastic process $\eta(\boldsymbol{z}) \in L_2(\Omega)$ with mean zero and covariance function $G_\eta(\boldsymbol{z}, \boldsymbol{z}') = \mathrm{Cov}\{\eta_i(\boldsymbol{z}), \eta_i(\boldsymbol{z}')\}$.

In this article, we present a comprehensive framework for estimation and inference of the mean function $\mu(\cdot)$ in model (1.1), along with theoretical support. Statistical inference is crucial in data-driven decision making as it accounts for the uncertainty

caused by noise in the data collected for complex objects. The prevailing analytic technique in 3D imaging analysis regards each voxel as a unit and makes a univariate statistical inference, as noted by Lazar (2008) and Nathoo et al. (2019) among others. In this case, many hypotheses are tested simultaneously, and the resulting multiple testing corrections are stringent. Furthermore, the resulting P-values are not independent because of spatial correlation in the complex object data. To address these challenges, we propose a novel technique for constructing simultaneous confidence corridors (SCCs) with guaranteed coverage probability to address the uncertainty in statistical inference for complex 3D objects. SCCs provide valuable insights into the global behavior of functions and can be used to identify significant regions, as well as quantify the difference between two groups. In medical imaging, SCCs can aid in locating effective regions in the images with high confidence and enhance the interpretability of results by visually representing effective regions, facilitating further analysis.

Several related studies on complex objects exist in the FDA literature. Petersen et al. (2019) introduced the Fréchet regression model, which utilizes the conditional Fréchet mean as a framework for regression analysis with responses that are metric space-valued objects and predictors that are Euclidean vectors. Dubey and Müller (2019) subsequently established the consistency of the sample Fréchet mean and derived a central limit theorem for the sample Fréchet variance, providing a means to quantify the variation around the Fréchet mean. Dai et al. (2018) considered an intrinsic principal component analysis for smooth Riemannian manifold-valued functional data and studied its asymptotic properties. Zhu et al. (2014) proposed a multiscale adaptive and sequential smoothing (MASS) method for studying the relationship between massive imaging data and a set of covariates of interest. While these studies have

explored the limiting distributions of the proposed estimators, they have not provided clear solutions for rigorous statistical inference.

In the literature, various methods have been proposed for constructing confidence bands for mean functions of 1D/2D functional data, such as simulation-based techniques (Degras, 2011; Cao et al., 2012b; Cao and Wang, 2018), functional principal component (FPC) based approach (Goldsmith et al., 2013), and geometric approach Choi and Reimherr (2018). Additionally, SCCs have also been developed for coefficient functions for varying coefficient models for 1D/2D functional responses (Zhu et al., 2012; Gu et al., 2014; Chang et al., 2017; Wang et al., 2020c). Despite these efforts, constructing SCCs for complex 3D data objects remains a challenge and, to the best of our knowledge, has not yet been addressed in the literature. In this article, we aim to fill this gap by providing the first attempt at constructing SCCs for the mean function of complex 3D objects.

Making inferences for complex 3D objects, such as the human brain in medical imaging, presents significant challenges due to their irregular and complex boundaries. These boundaries, which are not defined by simple geometric shapes like rectangles, make it difficult to apply traditional statistical methods. While conventional techniques such as kernel smoothing (Zhu et al., 2014), tensor smoothing (Li and Zhang, 2017) and wavelet smoothing (Morris and Carroll, 2006) may be used for 3D objects on rectangular domains, they often exhibit the "leakage problem." This issue refers to poor estimation performance over complex domains as information may be inappropriately borrowed across boundaries, resulting in inaccurate estimation. To address this issue, we consider using trivariate penalized spline smoothing based on triangulations (TPST) introduced in Li et al. (2022), which was specifically developed for smoothing data

collected from point clouds of arbitrary shapes. This TPST method is effective in handling complex domain boundaries, denoising, and preserving the inherent geometric features and spatial structures of the data, making it a promising solution for analyzing complex 3D objects.

To develop the SCC, efficient estimators for the covariance function $G_\eta(\boldsymbol{v}, \boldsymbol{v}')$ as well as the corresponding eigenvalue and eigenfunctions are necessary. Although various approaches to estimate these components have been proposed for 1D/2D functional data (Yao et al., 2005; Wang et al., 2020c), they are unsuitable for 3D functional objects due to several challenges. Firstly, the method requires a smoother for a 6D covariance function over a complex domain. Secondly, storing the covariances becomes increasingly difficult as the number of observations from each object grows. Lastly, traditional FPC analysis procedures become infeasible with a large amount of data. To tackle these challenges, we propose a novel and efficient method for estimating the model components. The approach can significantly accelerate the computation in FPC analysis and makes it feasible to process 3D objects with hundreds of thousands of observations.

In this paper, we propose an extension to the existing SCC construction procedure that allows for statistically quantifying differences between two sets of imaging data, which is often encountered in medical imaging studies. Our method provides a way to identify and locate regions where significant differences exist between the two groups. The proposed spline estimator and accompanying SCC have been shown to be asymptotically equivalent to the ideal scenario with known actual signal and computationally efficient even for large data volumes. Furthermore, our simulation studies have demonstrated the correct coverage probability, ensuring that the probability of the true mean

function falling within the SCC is close to the nominal level. This framework provides improved precision in statistical inference for complex 3D object analysis, particularly in identifying significant regions.

The rest of the article is organized as follows. In Section 2, we describe the model setup based on the observed data, the TPST estimator of the mean function $\mu(\cdot)$ in model (1.1) and establish its asymptotic properties under the FDA framework. In Section 3, we propose asymptotic SCCs for the mean function based on the TPST estimators. The specific implementation details, including the selection of triangulation, spline basis functions and smoothing parameters in the TPST estimation, and estimation of other unknown components required for constructing the SCCs, are thoroughly discussed in Section 4. Simulation studies and comparisons with existing methods are presented in Section 5, and a case study on brain imaging is presented in Section 6. In Section 7, we conclude the article with some discussions. Technical proofs of theoretical results and additional results from the simulation studies are provided in the Supplementary Material.

2. Mean Function Estimation via Trivariate Penalized Spline Smoothing

In this section, we present an efficient smoothing technique for estimating the mean function in the functional regression model (1.1).

2.1 Discretization of the Functional Response and Model Setup

As mentioned, we consider observations from n complex objects over a 3D domain Ω. In many practical applications, the continuous response process $Y_i(\boldsymbol{z})$ is only observed on a discrete location grid points $\{\boldsymbol{z}_1, \boldsymbol{z}_2, \ldots, \boldsymbol{z}_N\}$, where $\boldsymbol{z}_j \in \Omega$ indicates the jth

location of observation. In the context of 3D imaging, $\boldsymbol{z}_j$ refers to the jth voxel of the image. The discretized observations for the ith object are represented as $\{Y_{ij} = Y_i(\boldsymbol{z}_j) : \boldsymbol{z}_j \in \Omega\}_{i=1,j=1}^{n,N}$. For clarity, we demonstrate our method with this uniform spacing setting below. However, it is important to note that this uniform spacing is not required. As long as the grid is sufficiently dense to ensure accurate numerical integration, our method will perform effectively regardless of the spacing pattern.

In classical FPC analysis, we often assume there is a spectral decomposition: $G_\eta(\boldsymbol{z}, \boldsymbol{z}') = \sum_{k=1}^{\infty} \lambda_k \psi_k(\boldsymbol{z}) \psi_k(\boldsymbol{z}')$, where the pairs of eigenvalue and eigenfunction sequences $\{\lambda_k, \psi_k(\boldsymbol{z})\}_{k=1}^{\infty}$ satisfy $\lambda_1 \geq \lambda_2 \geq \cdots \geq 0$, $\sum_{k=1}^{\infty} \lambda_k < \infty$, and $\{\psi_k(\cdot)\}_{k=1}^{\infty}$ constitute an orthonormal basis of $L^2(\Omega)$. Using the Karhunen-Lo'eve expansion, the functional random effect $\eta_i(\boldsymbol{z})$ in model (1.1) can be represented as $\eta_i(\boldsymbol{z}) = \sum_{k=1}^{\infty} \xi_{ik} \phi_k(\boldsymbol{z})$, where $\phi_k(\boldsymbol{z}) = \sqrt{\lambda_k} \psi_k(\boldsymbol{z})$, and the coefficients ξ_{ik}'s are the FPC scores, which have zero means, unit variance, and are mutually uncorrelated.

With the discretized data observations and the Karhunen-Lo'eve expansion, model (1.1) can be equivalently written as

$$Y_{ij} = \mu(\boldsymbol{z}_j) + \sum_{k=1}^{\infty} \xi_{ik} \phi_k(\boldsymbol{z}_j) + \sigma(\boldsymbol{z}_j) \varepsilon_{ij},$$

where $\mu(\cdot)$ is the unknown mean function, typically assumed to be smooth in the FDA framework, and $\varepsilon_{ij} = \varepsilon_i(\boldsymbol{z}_j)$. As aforementioned, complex 3D objects are typically collected on an irregular domain with arbitrary shape, and the TPST method proposed in Li et al. (2022) is one of the smoothing techniques that can effectively handle this type of complex objects. Below, we delve into the details of the estimation procedure, including triangulations, trivariate spline basis functions, and the construction of penalized spline estimators. The asymptotic results of the proposed mean estimator are also presented.

2.2 Trivariate Splines over Triangulations

In the following, let T be a tetrahedron, a 3D convex hull formed by four non-coplanar points. A collection of H tetrahedra, $\triangle = \{T_1, \ldots, T_H\}$, forms a triangulation of a polygonal domain $\Omega = \cup_{h=1}^{H} T_h$ when any two tetrahedra in $\triangle$ intersect at most at a vertex, edge, or triangular face. There are various triangulation algorithms for 3D domains, such as the MATLAB functions `delaunay`, `distmesh/distmeshnd` (Persson and Strang, 2004), the `TetGen` software (Si, 2015), and the `CGAL` library (Project, 2020).

Next, we provide a brief overview of trivariate splines over a triangulation. More in-depth descriptions can be found in Lai and Schumaker (2007) and Li et al. (2022). Consider a non-degenerate tetrahedron $T = \langle \boldsymbol{v}_1, \boldsymbol{v}_2, \boldsymbol{v}_3, \boldsymbol{v}_4 \rangle$, with vertices $\boldsymbol{v}_1$, $\boldsymbol{v}_2$, $\boldsymbol{v}_3$, and $\boldsymbol{v}_4$. For any point $\boldsymbol{z} \in \mathbb{R}^3$, there is a unique representation in the form $\boldsymbol{z} = b_1\boldsymbol{v}_1 + b_2\boldsymbol{v}_2 + b_3\boldsymbol{v}_3 + b_4\boldsymbol{v}_4$, with $b_1 + b_2 + b_3 + b_4 = 1$, where b_1, b_2, b_3 and b_4 are called the barycentric coordinates of the point $\boldsymbol{z}$ relative to the tetrahedron T. The Bernstein polynomials of degree d relative to tetrahedron T can be defined as $B_{ijkl}^{T,d}(\boldsymbol{z}) = d!/(i!j!k!l!)b_1^i b_2^j b_3^k b_4^l$. Then for any $T \in \triangle$, we can write the polynomial piece of spline s restricted on $T \in \triangle$ as $s|_T = \sum_{i+j+k+l=d} \gamma_{ijkl}^T B_{ijkl}^{T,d}$, where $\boldsymbol{\gamma}_T = \{\gamma_{ijkl}^T, i+j+k+l = d\}$ are called B-coefficients of s.

For a nonnegative integer r, let $\mathbb{C}^r(\Omega)$ be the set of all r-times continuously differentiable functions over Ω. Given a triangulation $\triangle$ and a positive integer $d \geq r$, let $\mathcal{S}_d^r(\triangle) = \{s \in \mathbb{C}^r(\Omega) : s|_T \in \mathbb{P}_d(T), T \in \triangle\}$ be a spline space of degree d and smoothness r over the triangulation $\triangle$, where $\mathbb{P}_d$ is the space of all polynomials of degree less than or equal to d. To simplify notation, we denote $\{B_m\}_{m \in \mathcal{M}}$ be the set of degree-d trivariate Bernstein basis polynomials for $\mathcal{S}_d^r(\triangle)$, where $\mathcal{M}$ is the index set for all the Bernstein basis polynomials. Then, for any function $s \in \mathcal{S}_d^r(\triangle)$, we can represent it by

the following basis expansion:

$$s(\boldsymbol{z}) = \sum_{m \in \mathcal{M}} B_m(\boldsymbol{z})\gamma_m = \boldsymbol{B}(\boldsymbol{z})^\top \boldsymbol{\gamma}, \tag{2.1}$$

where $\boldsymbol{\gamma}^\top = (\gamma_m, m \in \mathcal{M})$ is the spline coefficient vector.

2.3 Penalized Spline Estimators for the Mean Function

We propose estimating $\mu(\cdot)$ based on the pooled data from all n complex objects $\{Y_{ij}\}_{i=1,j=1}^{n,N}$ using the penalized spline method. To simplify notations, for any index $\boldsymbol{a} = (a_1, a_2, a_3)$ of order $|\boldsymbol{a}| = a_1 + a_2 + a_3$, we denote the derivatives of function s by $D^{\boldsymbol{a}}s = \partial^{|\boldsymbol{a}|}s/\partial_x^{a_1}\partial_y^{a_2}\partial_z^{a_3}$. We consider the following penalized least squares problem:

$$\min_{g \in S_d^r(\triangle)} \sum_{i=1}^{n}\sum_{j=1}^{N}\{Y_{ij} - g(\boldsymbol{z}_j)\}^2 + \rho_n \mathcal{E}(g), \tag{2.2}$$

where $\mathcal{E}(g) = \sum_{|\boldsymbol{a}|=2} \binom{2}{a_1}\binom{2-a_1}{a_2} \int_\Omega \{D^{\boldsymbol{a}}g(\boldsymbol{z})\}^2 \mathrm{d}\boldsymbol{z}$ is the roughness penalty, and ρ_n is the roughness penalty parameter.

To ensure smoothness in the splines, linear constraints must be imposed on the spline coefficients $\boldsymbol{\gamma}$ in (2.1). These constraints are satisfied by requiring $\boldsymbol{\gamma}$ to satisfy $\mathbf{H}\boldsymbol{\gamma} = \mathbf{0}$, where $\mathbf{H}$ is the matrix representing the smoothness conditions across shared edges or faces of tetrahedra, and depends on the smoothness parameter r and the structure of the triangulation. As a result, the minimization problem in (2.2) becomes

$$\sum_{i=1}^{n}\sum_{j=1}^{N}\{Y_{ij} - \mathbf{B}^\top(\boldsymbol{z}_j)\boldsymbol{\gamma}\}^2 + \rho_n \boldsymbol{\gamma}^\top \mathbf{P}\boldsymbol{\gamma}, \text{ subject to } \mathbf{H}\boldsymbol{\gamma} = \mathbf{0}, \tag{2.3}$$

where the block diagonal penalty matrix $\mathbf{P}$ satisfies $\boldsymbol{\gamma}^\top\mathbf{P}\boldsymbol{\gamma} = \mathcal{E}(\mathbf{B}\boldsymbol{\gamma})$; see Li et al. (2022) for the exact form of $\mathbf{P}$.

To eliminate the constraints, we employ the QR decomposition. This results in $\mathbf{H}^\top = \mathbf{Q}\mathbf{R}$, where $\mathbf{Q}$ is orthogonal and $\mathbf{R}$ is an upper triangular matrix. Let p denote

the rank of $\mathbf{H}$. The first p columns of $\mathbf{Q}$ are represented by $\mathbf{Q}_1$, while $\mathbf{R}_2$ is a matrix of zeros. Then, we have $\mathbf{H}^\top = (\mathbf{Q}_1\ \mathbf{Q}_2)\binom{\mathbf{R}_1}{\mathbf{R}_2}$. The condition $\mathbf{H}\boldsymbol{\gamma} = \mathbf{0}$ is equivalent to the existence of $\boldsymbol{\theta}$ such that $\boldsymbol{\gamma} = \mathbf{Q}_2\boldsymbol{\theta}$. Denote $\bar{Y}_{\cdot,j} = n^{-1}\sum_{i=1}^{n} Y_{ij}$, $\bar{\mathbf{Y}} = (\bar{Y}_{\cdot,1}, \ldots, \bar{Y}_{\cdot,N})^\top$, $\mathbf{U} = \mathbf{B}\mathbf{Q}_2$, and $\mathbf{D} = \mathbf{Q}_2^\top\mathbf{P}\mathbf{Q}_2$. With these definitions, the minimization problem in (2.3) can be converted to a penalized regression problem that is free of constraints:

$$\left\|\bar{\mathbf{Y}} - \mathbf{B}\mathbf{Q}_2\boldsymbol{\theta}\right\|^2 + \frac{\rho_n}{n}\boldsymbol{\theta}^\top\mathbf{Q}_2^\top\mathbf{P}\mathbf{Q}_2\boldsymbol{\theta} = \left\|\bar{\mathbf{Y}} - \mathbf{U}\boldsymbol{\theta}\right\|^2 + \frac{\rho_n}{n}\boldsymbol{\theta}^\top\mathbf{D}\boldsymbol{\theta}, \tag{2.4}$$

and the minimizer of (2.4) is given by $\widehat{\boldsymbol{\theta}} = (\mathbf{U}^\top\mathbf{U} + n^{-1}\rho_n\mathbf{D})^{-1}\mathbf{U}^\top\bar{\mathbf{Y}}$. Thus, the estimator of $\boldsymbol{\gamma}$ and $\mu(\cdot)$ are $\widehat{\boldsymbol{\gamma}} = \mathbf{Q}_2\widehat{\boldsymbol{\theta}}$ and $\widehat{\mu}(\boldsymbol{z}) = \mathbf{B}^\top(\boldsymbol{z})\widehat{\boldsymbol{\gamma}}$, respectively.

2.4 Convergence of the Penalized Estimators

In this section, we examine the asymptotic behavior of the proposed trivariate spline estimator $\widehat{\mu}(\cdot)$. We begin by introducing some necessary notations and definitions. According to (Lai and Wang, 2013), for a non-degenerate tetrahedron $T \in \triangle$, we let $|T|$ denote its longest edge length, and ϱ_T be the radius of the largest ball that can be inscribed in T. The shape parameter of T is then defined as $\pi_T = |T|/\varrho_T$. The size of $\triangle$ is given by $|\triangle| := \max\{|T|, T \in \triangle\}$, which is the length of the longest edge. Let $g(\boldsymbol{z})$ be a function defined on the closure of the domain Ω. The regular L^2 norm of g is denoted as $\|g\|_{L^2(\Omega)}$, given by $\|g\|_{L^2(\Omega)} = \{\int_\Omega g^2(\boldsymbol{z})\mathrm{d}\boldsymbol{z}\}^{1/2}$. The supremum norm of g is denoted as $\|g\|_{\infty,\Omega}$ and is defined as $\|g\|_{\infty,\Omega} = \sup_{\boldsymbol{z}\in\Omega}|g(\boldsymbol{z})|$. In addition, we use $|g|_{\upsilon,\infty,\Omega} = \sum_{|\boldsymbol{a}|\leq\upsilon}\|D^{\boldsymbol{a}}g\|_{L^q(\Omega)}$ to denote the maximum norms of all the υth order derivatives of g over Ω. For $1 \leq q \leq \infty$ and $\ell \geq 1$, let $\mathcal{W}^{\ell,q}(\Omega) = \{g : |g|_{k,q,\Omega} < \infty, 0 \leq k \leq \ell\}$ be the standard Sobolev space. We next introduce some technical conditions.

(A1) The trivariate function $\mu \in \mathcal{W}^{\ell+1,\infty}(\Omega)$ for an integer $\ell \geq 1$.

(A2) For any $k \geq 1$, ξ_{ik}'s are i.i.d. random variables with zero mean, unit variance, and $\mathrm{E}|\xi_{ik}|^{4+\delta_1} < +\infty$ for some constant $\delta_1 > 0$. For any $i = 1, \ldots, n$, $j = 1, \ldots, N$, ε_{ij}'s are i.i.d with zero mean, unit variance, and $\mathrm{E}|\varepsilon_{ij}|^{4+\delta_2} < +\infty$ for some constant $\delta_2 > 0$.

(A3) For any $\boldsymbol{z} \in \Omega$, $\sigma(\boldsymbol{z}) \in \mathcal{C}^{(1)}(\Omega)$ with $0 < c_\sigma \leq \sigma(\boldsymbol{z}) \leq C_\sigma \leq \infty$; for any k, $\psi_k(\boldsymbol{z}) \in \mathcal{C}^{(1)}(\Omega)$ and the variance function $0 < c_G \leq G_\eta(\boldsymbol{z}, \boldsymbol{z}) \leq C_G \leq \infty$.

(A4) The triangulations is π-quasi-uniform, that is, there exists a positive constant π such that $(\min_{T \in \triangle} \varrho_T)^{-1} |\triangle| \leq \pi$.

(A5) As $N \to \infty$, $n \to \infty$, $N^{-1} n^{3/2(\ell+1)} \log(n) \to 0$, the triangulation size satisfies that $N^{-1} \log(n) \ll |\triangle|^3 \ll \min\{n^{(2+\delta_2)/(4+\delta_2)} N^{-1} \log^{-1}(n), n^{-3/(2\ell+2)}\}$, and penalty parameter $\rho_n = o\{\min(n^{1/2} N |\triangle|^{7/2}, n N^{3/2} |\triangle|^7, n N |\triangle|^{11/2})\}$.

The above conditions are reasonable and commonly assumed in the literature. Assumption (A1) is a standard requirement for the true underlying functions in non-parametric estimation. It can be relaxed to $\mu(\cdot) \in \mathcal{C}^{(0)}(\Omega)$ if the underlying signal from the complex objects is not very smooth. Assumptions (A2) and (A3) are commonly used in the field, as seen in Cao et al. (2012b), Cao et al. (2012a), Wang et al. (2020c), Yu et al. (2021) and Li et al. (2021). Assumption (A4) suggests using more uniformly spaced triangulations with smaller shape parameters; see Lai and Wang (2013); Li et al. (2022). This assumption emphasizes the importance of well-shaped triangles, without small or obtuse angles, to ensure numerical stability and accurate representation of the domain. Assumption (A5) imposes a condition on the relationship between the number of objects n and the number of observations N per object and specifies the required growth rate of the spline space dimension relative to n and N. This requirement aligns

with established practices in 1D and 2D FDA settings (Wang et al., 2020a,c), and can guide us in determining the appropriate level of triangulation fineness.

The convergence rate of $\widehat{\mu}(\cdot)$ is provided Theorem 1 for both L^2 and uniform convergence. Please refer to the Supplementary Material for a detailed proof of this theorem.

Theorem 1. *Suppose Assumptions (A1)–(A4) are satisfied and* $N^{1/3}|\triangle| \to \infty$ *as* $N \to \infty$. *Then, the TPST estimator of* $\mu(\cdot)$ *is consistent and satisfies*

$$\|\widehat{\mu} - \mu\|_{L^2} = O_P\left\{\frac{\rho_n}{nN|\triangle|^{7/2}}|\mu|_{2,\infty,\Omega} + \left(1 + \frac{\rho_n}{nN|\triangle|^{11/2}}\right)|\triangle|^{\ell+1}|\mu|_{\ell+1,\infty,\Omega} + \frac{1}{\sqrt{n}} + \frac{1}{\sqrt{nN}|\triangle|^{3/2}}\right\}.$$

In addition, if Assumption (A5) holds, we have $\|\widehat{\mu} - \mu\|_\infty = O_P\{n^{-1/2}\log^{1/2}(n)\}$ *and* $\|\widehat{\mu} - \mu\|_{L^2} = O_P(n^{-1/2})$.

Remark 1. Theorem 1 provides the convergence rate of the TPST estimator $\widehat{\mu}(\cdot)$ to the true mean function $\mu(\cdot)$. The first term in the order of $\|\widehat{\mu} - \mu\|_{L^2}$ shows the bias brought by the roughness penalty. When the tuning parameter is sufficiently small, the second term represents the bias arising from approximating an arbitrary function μ using a trivariate spline. The last two terms demonstrate the estimation variances arising from the individual variations η_i and random noise ε_i.

Note that various factors, such as the refinement of the triangulation, the smoothness and degree of the trivariate spline, the choice of penalty parameter, and the characteristics of the unknown mean function influence the convergence rate. As discussed in Section 5, the polynomial degree d and the triangulation size $|\triangle|$ have a direct impact on computational demands. This result also provides a guideline on how to choose the triangulation. As the sample size increases and more data points become available, a finer triangulation can be considered for a more accurate estimation of the mean

function. In addition, a finer triangulation is needed when there are rapid changes in the mean function or when the domain is highly curved or complex.

Remark 2. Theorem 1 also highlights the impact of the "curse of dimensionality" on the convergence rate of the TPST estimator for the mean function of 3D images, in comparison to the BPST estimator for the mean function of 2D images introduced in Wang et al. (2020c). Specifically, when considering data observed on a 2D domain, the BPST estimator for the mean function $\mu(\boldsymbol{z})$, $\boldsymbol{z} \in \mathbb{R}^2$, exhibits a faster convergence rate, represented as $O_P\left\{\frac{\rho_n}{nN|\triangle|^3}|\mu|_{2,\infty,\Omega} + \left(1+\frac{\rho_n}{nN|\triangle|^5}\right)|\triangle|^{\ell+1}|\mu|_{\ell+1,\infty,\Omega} + n^{-1/2} + (nN)^{-1/2}|\triangle|^{-1}\right\}$, where N is the number of observations in one 2D object, and $|\triangle|$ is the size of the 2D triangulation. On the other hand, the TPST estimator proposed in this paper for the mean function $\mu(\boldsymbol{z})$ in 3D objects, where $\boldsymbol{z} \in \mathbb{R}^3$, exhibits a slower convergence rate.

3. Simultaneous Confidence Corridors (SCCs)

In this section, we build upon the TPST estimators in Section 2 to develop SCCs to quantify the uncertainty associated with the estimators. We begin by constructing SCCs for the mean function in a one-sample scenario and propose an efficient FPC method to estimate the required covariance function and associated eigen components. We then expand our results to a two-sample scenario, providing a solution for characterizing differences between the mean functions of two groups of complex objects.

3.1 One-sample SCC

We start by considering the covariance operator $G_\eta(\boldsymbol{z}, \boldsymbol{z}') = \sum_{k=1}^{\kappa} \lambda_k \psi_k(\boldsymbol{z})\psi_k(\boldsymbol{z}')$ for $\boldsymbol{z},\ \boldsymbol{z}' \in \Omega$. We define a standardized Gaussian process $\zeta(\boldsymbol{z})$ with zero mean and unit variance such that $\mathrm{E}\zeta(\boldsymbol{z}) = 0$, $\mathrm{E}\zeta^2(\boldsymbol{z}) = 1$, and covariance function $\mathrm{E}\zeta(\boldsymbol{z})\zeta(\boldsymbol{z}') =$

$G_\eta(\boldsymbol{z},\boldsymbol{z}')\{G_\eta(\boldsymbol{z},\boldsymbol{z})G_\eta(\boldsymbol{z}',\boldsymbol{z}')\}^{-1/2}$, $\boldsymbol{z},\boldsymbol{z}' \in \Omega$. We denote the $100(1-\alpha)$th percentile of the distribution of the absolute maximum of $\zeta(\boldsymbol{z})$ as $q_{1-\alpha}$, such that $P\{\sup_{\boldsymbol{z}\in\Omega}|\zeta(\boldsymbol{z})| \leq q_{1-\alpha}\} = 1-\alpha$ for $\alpha \in (0,1)$.

To explore theoretical properties, we define an "oracle" estimator $\bar{\mu}(\boldsymbol{z}) = \mu(\boldsymbol{z}) + n^{-1}\sum_{i=1}^{n}\eta_i(\boldsymbol{z})$. Obviously, obtaining the true value of $\bar{\mu}(\boldsymbol{z})$ is impossible since the data are only observed on the finite location grid points $\{\boldsymbol{z}_j : j = 1,\ldots,N\}$ and are subject to noise. To demonstrate that the difference between the TPST estimator and the oracle estimator is negligible, we further make the following assumption.

(A6) For $k \in \{1,\ldots,\kappa\}$ and an integer $s \geq 0$, $\phi_k(\boldsymbol{z}) \in \mathcal{W}^{s+1,\infty}(\Omega)$, $\sum_{k=1}^{\kappa}\|\phi_k\|_\infty < \infty$. $\rho_n n^{-1}N^{-1}|\triangle|^{-7/2}\sum_{k=1}^{\kappa_n}\|\phi_k\|_{2,\infty} = o(1)$, $(1+\rho_n n^{-1}N^{-1}|\triangle|^{-11/2})\sum_{k=1}^{\kappa_n}|\triangle|^{s+1}\|\phi_k\|_{s+1,\infty} = o(1)$ for a sequence $\{\kappa_n\}_{n=1}^{\infty}$ of increasing integers, with $\lim_{n\to\infty}\kappa_n = \kappa$. Meanwhile, $\sum_{k=\kappa_n+1}^{\kappa}\|\phi_k\|_\infty = o(1)$. The number κ of nonzero eigenvalues is finite or κ is infinite while the variables ξ_{ik}'s are i.i.d. for $1 \leq i < \infty, 1 \leq k < \infty$.

Assumption (A6) emphasizes the smoothness requirement of the FPCs and the i.i.d. condition of FPC scores ξ_{ik}'s is used to demonstrate the oracle efficiency of the proposed estimator.

Theorem 2. *Under Assumptions (A1)–(A6), for any $\alpha \in (0,1)$, as $N \to \infty$ and $n \to \infty$, $P\left\{\sup_{\boldsymbol{z}\in\Omega} n^{1/2}|\bar{\mu}(\boldsymbol{z}) - \mu(\boldsymbol{z})|G_\eta(\boldsymbol{z},\boldsymbol{z})^{-1/2} \leq q_{1-\alpha}\right\} \to 1-\alpha$ and $\sup_{\boldsymbol{z}\in\Omega}|\bar{\mu}(\boldsymbol{z}) - \widehat{\mu}(\boldsymbol{z})| = o_P(n^{-1/2})$.*

Remark 3. Theorem 2 explores the asymptotic properties of the "oracle" estimator. Specifically, as the sample size n increases, the probability that the uniform difference between the sample mean function and the true mean function, scaled by the standard deviation of the estimation error, does not exceed the critical value $q_{1-\alpha}$ approaches

$1-\alpha$. Therefore, we have $P\left\{\mu(\boldsymbol{z}) \in \bar{\mu}(\boldsymbol{z}) \pm n^{-1/2} q_{1-\alpha} G_\eta(\boldsymbol{z},\boldsymbol{z})^{1/2},\ \boldsymbol{z} \in \Omega\right\} \to 1-\alpha$, as $n \to \infty$. In addition, the theorem shows that the uniform bound of difference between the TPST estimator $\widehat{\mu}(\cdot)$ and the "oracle" smoother $\bar{\mu}(\cdot)$ is at $o_P(n^{1/2})$ rate. That is, the TPST estimator $\widehat{\mu}(\cdot)$ is oracally efficient.

Using Theorems 1 and 2, we can derive the following asymptotic SCCs for $\mu(\boldsymbol{z})$ over $\boldsymbol{z} \in \Omega$.

Corollary 1. *Suppose Assumptions (A1)–(A6) hold. For any $\alpha \in (0,1)$, as $N \to \infty$ and $n \to \infty$, an asymptotic $100(1-\alpha)\%$ exact SCC for $\mu(\boldsymbol{z})$ is*

$$P\left\{\mu(\boldsymbol{z}) \in \widehat{\mu}(\boldsymbol{z}) \pm n^{-1/2} q_{1-\alpha} G_\eta(\boldsymbol{z},\boldsymbol{z})^{1/2},\ \boldsymbol{z} \in \Omega\right\} \to 1-\alpha.$$

3.2 Estimation of FPC analysis

In practice, to construct SCCs as derived in Section 3.1, it is necessary to estimate the FPC, such as the variance-covariance function $G_\eta(\boldsymbol{z},\boldsymbol{z}')$ and its eigenvalues and eigenfunctions.

For any object $i = 1,\ldots,n$ and grid point $j = 1,\ldots,N$, we calculate the residual by $\widehat{R}_{ij} = Y_{ij} - \widehat{\mu}(\boldsymbol{z}_j)$. Then, we apply the TPST smoothing method again to these residuals $\{(\widehat{R}_{ij}, \boldsymbol{z}_j)\}_{j=1}^N$ to obtain an estimator for each $\eta_i(\boldsymbol{z})$. Specifically, for each $i = 1,\ldots,n$, we define the TPST estimator of $\eta_i(\boldsymbol{z})$ as

$$\widehat{\eta}_i(\boldsymbol{z}) = \underset{g_i \in \mathcal{S}_d^r(\triangle^*)}{\arg\min} \sum_{j=1}^{N} \left\{\widehat{R}_{ij} - g_i(\boldsymbol{z}_j)\right\}^2 + \rho_n^* \mathcal{E}(g_i), \tag{3.1}$$

where the triangulation $\triangle^*$ and smoothness penalty ρ_n^* used to estimate $\eta_i(\boldsymbol{z})$ in this context may differ from those introduced in Section 2.

Let $\widehat{\eta}_i(\boldsymbol{z}) = \sum_{m \in \widetilde{\mathcal{M}}} \widetilde{B}_m(\boldsymbol{z}) \widehat{\gamma}_m^{(i)}$ be the TPST estimator defined in (3.1) and let

$\widehat{\beta}_{mm'} = n^{-1}\sum_{i=1}^{n}\widehat{\gamma}_m^{(i)}\widehat{\gamma}_{m'}^{(i)}$. We can estimate $G_\eta(\cdot,\cdot)$ by

$$\widehat{G}_\eta(\boldsymbol{z},\boldsymbol{z}') = n^{-1}\sum_{i=1}^{n}\widehat{\eta}_i(\boldsymbol{z})\widehat{\eta}_i(\boldsymbol{z}') = \sum_{m\in\widetilde{\mathcal{M}}}\sum_{m'\in\widetilde{\mathcal{M}}}\widehat{\beta}_{mm'}\widetilde{B}_m(\boldsymbol{z})\widetilde{B}_{m'}(\boldsymbol{z}'), \tag{3.2}$$

and we estimate the eigenfunctions $\psi_k(\cdot)$ using the following eigenequations:

$$\int_\Omega \widehat{G}_\eta(\boldsymbol{z},\boldsymbol{z}')\widehat{\psi}_k(\boldsymbol{z})\mathrm{d}\boldsymbol{z} = \widehat{\lambda}_k\widehat{\psi}_k(\boldsymbol{z}'), \tag{3.3}$$

where $\widehat{\psi}_k$'s satisfy $\int_\Omega \widehat{\psi}_k^2(\boldsymbol{z})\mathrm{d}\boldsymbol{z} = 1$ and $\int_\Omega \widehat{\psi}_k(\boldsymbol{z})\widehat{\psi}_{k'}(\boldsymbol{z})\mathrm{d}\boldsymbol{z} = 0$ for $k' < k$. If N is sufficiently large, the left hand side of (3.3) can be approximated by $\sum_{j=1}^{N}\widehat{G}_\eta(\boldsymbol{z}_j,\boldsymbol{z}_{j'})\widehat{\psi}_k(\boldsymbol{z}_j)A(\boldsymbol{z}_j)$, where $A(\boldsymbol{z}_j)$ is the volume of the voxel $\boldsymbol{z}_j$.

Theorem 3 below characterizes the uniform weak convergence of $\widehat{G}_\eta(\boldsymbol{z},\boldsymbol{z}')$ and the convergence of $\widehat{\psi}_k$ and $\widehat{\lambda}_k$. To establish Theorem 3, we require the following additional assumption, which outlines the requirements for sample size and the triangulation method employed to obtain the TPST estimator of $\{\eta_i\}_{i=1}^n$ as presented in (3.1).

(A7) As $N\to\infty$, $n\to\infty$, for some $0<\delta_3<1$ and $s\geq 0$ given in Assumption (A6), $N^{-1}n^{1/(s+1)+\delta_3}\to 0$, $N|\triangle_\eta|^3\to\infty$, and $n^2|\triangle_\eta|^6/\log n\to\infty$, where $\triangle_\eta$ is the triangulation used to obtain the TPST estimator of η_i, $i=1,\ldots,n$, in (3.1).

Theorem 3. *Under Assumptions (A1)–(A7), we have the following results:*

(i) The spline estimator $\widehat{G}_\eta(\boldsymbol{z},\boldsymbol{z}')$ in (3.2) uniformly converges to $G_\eta(\boldsymbol{z},\boldsymbol{z}')$ in probability, i.e., $\sup_{(\boldsymbol{z},\boldsymbol{z}')\in\Omega^2}|\widehat{G}_\eta(\boldsymbol{z},\boldsymbol{z}') - G_\eta(\boldsymbol{z},\boldsymbol{z}')| = o_P(1)$.

(ii) $\|\widehat{\psi}_k - \psi_k\| = o_P(1)$, $|\widehat{\lambda}_k - \lambda_k| = o_P(1)$, for $k = 1,\ldots,\kappa$.

Even though there is an infinite number of terms in the Karhunen-Loéve representation of the covariance function theoretically, in FPC applications, it is common to

truncate the spectral decomposition at an integer κ. This integer is often chosen to account for a predetermined proportion of the variance (Hall et al., 2006; Li et al., 2013). Alternatively, one can select the number of the principal components using the Akaike information criterion (AIC) suggested by Yao et al. (2005), or the Bayesian information criterion (BIC) proposed by Li et al. (2013). In our subsequent numerical studies, we select κ as the number of eigenvalues required to explain 95% of the variation observed in the data.

After κ is determined, we consider the following spline approximation for $\psi_k(\cdot)$. Let $\widetilde{\mathbf{B}}(\boldsymbol{z}) = \{\widetilde{B}_m(\boldsymbol{z})\}_{m\in\widetilde{\mathcal{M}}}^\top$, and denote $\widetilde{\mathbf{B}} = \left\{\widetilde{\mathbf{B}}(\boldsymbol{z}_1), \ldots, \widetilde{\mathbf{B}}(\boldsymbol{z}_N)\right\}^\top$. Then, for any $k = 1, \ldots, \kappa$, we can approximate $\psi_k(\cdot)$ by $\widehat{\psi}_k(\boldsymbol{z}) = \sum_{m\in\widetilde{\mathcal{M}}} \widehat{\alpha}_{km}\widetilde{B}_m(\boldsymbol{z})$, where $\widehat{\alpha}_{km}$'s are coefficients of the spline estimator subject to $\widehat{\boldsymbol{\alpha}}_k^\top \widetilde{\mathbf{B}}^\top \widetilde{\mathbf{B}} \widehat{\boldsymbol{\alpha}}_k = N$ with $\widehat{\boldsymbol{\alpha}}_k = (\widehat{\alpha}_{k1}, \ldots, \widehat{\alpha}_{k|\widetilde{\mathcal{M}}|})^\top$. The estimates of eigenfunctions and eigenvalues correspond ψ_k and λ_k can be obtained by solving the eigenequations,

$$\int \widehat{G}_\eta(\boldsymbol{z}, \boldsymbol{z}')\widehat{\psi}_k(\boldsymbol{z}')\mathrm{d}\boldsymbol{z}' = \widehat{\lambda}_k\widehat{\psi}_k(\boldsymbol{z}), \quad k = 1, \ldots, \kappa. \tag{3.4}$$

By Equation (3.2), solving (3.4) is equivalent to solve, for $k = 1, \ldots, \kappa$,

$$\sum_{m\in\widetilde{\mathcal{M}}}\sum_{m'\in\widetilde{\mathcal{M}}}\sum_{l\in\widetilde{\mathcal{M}}} \widehat{\alpha}_{kl}\widehat{\beta}_{mm'}\widetilde{B}_m(\boldsymbol{z}) \int \widetilde{B}_{m'}(\boldsymbol{z}')\widetilde{B}_l(\boldsymbol{z}')\mathrm{d}\boldsymbol{z}' = \widehat{\lambda}_k \sum_{m\in\widetilde{\mathcal{M}}} \widehat{\alpha}_{km}\widetilde{B}_m(\boldsymbol{z}),$$

that is, let $\widehat{\boldsymbol{\beta}} = \{\widehat{\beta}_{mm'}\}_{m,m'\in\widetilde{\mathcal{M}}}$, then $N^{-1}\widetilde{\mathbf{B}}(\boldsymbol{z})^\top\widehat{\boldsymbol{\beta}}\widetilde{\mathbf{B}}^\top\widetilde{\mathbf{B}}\widehat{\boldsymbol{\alpha}}_k = \widehat{\lambda}_k\widetilde{\mathbf{B}}(\boldsymbol{z})^\top\widehat{\boldsymbol{\alpha}}_k$. By simple algebra, one needs to solve $N^{-1}\widehat{\boldsymbol{\beta}}\widetilde{\mathbf{B}}^\top\widetilde{\mathbf{B}}\widehat{\boldsymbol{\alpha}}_k = \widehat{\lambda}_k\widehat{\boldsymbol{\alpha}}_k$, for any $k = 1, \ldots, \kappa$. Consider the following Cholesky decomposition: $\widetilde{\mathbf{B}}^\top\widetilde{\mathbf{B}} = \mathbf{L}_B\mathbf{L}_B^\top$. Therefore, solving (3.4) is equivalent to solve $\widehat{\lambda}_k\mathbf{L}_B^\top\widehat{\boldsymbol{\alpha}}_k = N^{-1}\mathbf{L}_B^\top\widehat{\boldsymbol{\beta}}\mathbf{L}_B\mathbf{L}_B^\top\widehat{\boldsymbol{\alpha}}_k$, that is, $\widehat{\lambda}_k$ and $N^{-1/2}\mathbf{L}_B^\top\widehat{\boldsymbol{\alpha}}_k$, $k = 1, \ldots, \kappa$, are the eigenvalues and unit eigenvectors of $N^{-1}\mathbf{L}_B^\top\widehat{\boldsymbol{\beta}}\mathbf{L}_B$, satisfying that $\|N^{-1/2}\mathbf{L}_B^\top\widehat{\boldsymbol{\alpha}}_k\|^2 = 1$. In other words, $\widehat{\boldsymbol{\alpha}}_k$ is obtained by multiplying $N^{1/2}(\mathbf{L}_B^\top)^{-1}$ immediately after the unit eigenvectors of $N^{-1}\mathbf{L}_B^\top\widehat{\boldsymbol{\beta}}\mathbf{L}_B$, hence $\widehat{\psi}_k(\cdot)$ is obtained.

3.3 Statistical Comparison of Two Independent Groups Using SCCs

While one-sample SCCs are often the focus of many analyses, there are cases where it is also essential to compare two groups, such as healthy control subjects versus patients. In this section, we expand our method to cover two-sample problems and build SCCs for the difference between the mean functions of two independent groups, similar to a two-sample t-test. These two-sample SCCs enable us to evaluate the differences between two groups with quantified uncertainty.

Suppose we have two groups of objects, each with sample sizes n_1 and n_2, respectively, defined on a common region Ω. For group $H = 1, 2$, let $G_{H\eta}(\boldsymbol{z}, \boldsymbol{z}') = \sum_{k=1}^{\kappa} \phi_{Hk}(\boldsymbol{z})\phi_{Hk}(\boldsymbol{z}')$ be a positive definite function and $\widehat{\mu}_H(\cdot)$ be the spline estimates for the group mean function $\mu_H(\cdot)$.

Let $V(\boldsymbol{z}, \boldsymbol{z}') = G_{1\eta}(\boldsymbol{z}, \boldsymbol{z}') + \tau G_{2\eta}(\boldsymbol{z}, \boldsymbol{z}')$, where $\tau = \lim_{n_1 \to \infty} n_1/n_2$. We define $W(\boldsymbol{z})$, $\boldsymbol{z} \in \Omega$, as a standardized Gaussian process with mean 0, variance 1, covariance $\mathrm{E}[W(\boldsymbol{z})W(\boldsymbol{z}')] = \{V(\boldsymbol{z}, \boldsymbol{z})\}^{-1/2} V(\boldsymbol{z}, \boldsymbol{z}')\{V(\boldsymbol{z}', \boldsymbol{z}')\}^{-1/2}$, and denote $q_{12,\alpha}$ as the $(1-\alpha)$-th quantile of the absolute maximal distribution of $W(\boldsymbol{z})$.

Theorem 4. *Suppose Assumptions (A1)–(A6) hold. For any $\alpha \in (0, 1)$, as $n_1,\ n_2 \to \infty$, $\lim n_1/n_2 \to \tau > 0$,*

$$P\left\{ \sup_{\boldsymbol{z} \in \Omega} \frac{n_1^{1/2} |(\widehat{\mu}_1 - \widehat{\mu}_2)(\boldsymbol{z}) - (\mu_1 - \mu_2)(\boldsymbol{z})|}{\sqrt{V(\boldsymbol{z}, \boldsymbol{z})}} \leq q_{12,\alpha} \right\} \to 1 - \alpha.$$

Remark 4. According to Theorem 4, we can construct an asymptotic $100(1-\alpha)\%$ exact SCC for $(\mu_1 - \mu_2)(\boldsymbol{z})$ as $(\widehat{\mu}_1 - \widehat{\mu}_2)(\boldsymbol{z}) \pm n_1^{-1/2} q_{12,\alpha}\{V(\boldsymbol{z}, \boldsymbol{z})\}^{1/2}$.

Remark 5. It is important to note that the assumption of equal resolution for objects from both groups is made for the simplicity of the proof. However, this assumption can be relaxed without significantly affecting the validity of the theorem. In practical

applications, it is not uncommon for objects collected from different groups to have different spatial resolutions, and Theorem 4 can still be applied in such scenarios by making necessary modifications.

4. Implementation

In this section, we address the key considerations in selecting the triangulation, spline basis, and penalty parameters in the TPST estimation, and provide systematic and effective strategies for choosing these parameters. Furthermore, we provide a procedure for constructing the SCCs described in Section 3 and propose a modification to deal with situations where the measurement errors do not satisfy the assumptions. This modification allows for a more robust and practical application of the SCC method to a broader range of analysis scenarios.

4.1 Triangulation Selection

The selection of an appropriate triangulation is a crucial aspect of estimating the mean functions μ and the individual variation function $\eta_i(\cdot)$, as well as constructing the SCCs. Several factors influence the level of triangulation required to estimate the regression function accurately. One such factor is the inherent complexity of the domain itself. 3D domains characterized by high curvature or intricate shapes typically necessitate a finer triangulation.

According to Theorem 1, the characteristics of the function being estimated also play a vital role in selecting the level of triangulation. Functions with rapid changes or localized features may require finer triangulation to capture these nuances accurately. Moreover, Theorem 1 also indicates that the number of objects n and the number of

observations N per object impact the appropriate level of triangulation. With larger n and N, finer triangulation can be considered to attain more precise estimations of the target function. However, to ensure reliable estimation, it is recommended that each tetrahedron contains a minimum of $\lfloor \binom{d+3}{3}/2 \rfloor$ observations, depending on degree d of the spline basis.

To strike a balance between accuracy and computational efficiency in the estimation, we suggest prioritizing a finer triangulation when estimating the overall mean function μ compared to the individual variation η_i. This is because the mean function represents the overall trend or pattern in the data, and its accuracy is typically crucial in constructing the SCC. Finer triangulation helps capture the subtle variations and details in the mean function, which may lead to a more precise estimation. However, this doesn't mean we need to choose a really fine triangulation. The theoretical findings from Section 3 indicate that the choice of triangulation has a minimal effect on the performance of the TSSS estimator as long as the triangulation is fine enough to capture the underlying pattern. On the other hand, η_i describes the individual variation from the mean function. While it is still important to obtain a reasonably accurate estimation, it often exhibits more localized variations and may require a different level of detail than the mean function. Therefore, a coarser triangulation can be used to estimate η_i, as long as it adequately captures the major patterns and variations.

4.2 Spline Basis Selection

Selecting the spline basis is generally more manageable than choosing the triangulation. The parameters for the spline space $\mathcal{S}_d^r(\triangle)$, specifically d and r, can be predetermined by the user or chosen using techniques such as K-fold cross-validation (CV) or general-

ized cross-validation (GCV). For a fixed triangulation, we consider a sequence of values $d = 2, 3, \ldots, 9$. For each value of d, a TPST estimator can be obtained by selecting the smoothing parameter λ that minimizes the GCV as described in Section 4.3, and we choose d that minimizes the GCV. Simulation studies in Section 5 and Section S1 of the Supplementary Material provide evidence that the choice of d may impact the accuracy of the estimator. Specifically, a higher value of d provides greater flexibility in the estimator but increases the risk of overfitting. Conversely, a lower value of d may lead to underfitting and insufficient capture of the true underlying pattern.

Similar to the choice of triangulation, it is advisable to use a higher value of d when the goal is to enhance accuracy and capture local structures in the estimation of the mean function. This allows for a more detailed representation of the complex features in the data. On the other hand, when estimating the individual variation η_i, it may be more appropriate to employ a slightly oversmoothed function achieved by using a lower degree of d. This can help reduce noise and highlight the overall trends in the individual variation while avoiding excessive complexity.

Similarly, the smoothness condition r also affects the estimation accuracy and computational complexity. In practice, commonly used smoothness conditions include $r = 0$ and $r = 1$. A higher smoothness condition (such as $r = 1$) results in smoother estimates but may oversmooth the data, leading to the loss of important details. Conversely, a lower smoothness condition (such as $r = 0$) allows for more flexibility in capturing local variations but may result in a rougher estimation. The choice of r should be guided by the specific characteristics of the data and the desired trade-off between smoothness and fidelity to the underlying patterns.

4.3 Roughness Penalty Parameter Selection

A suitable value of the roughness penalty parameter ρ_n needs to be chosen to achieve a good fit of the data. A smoother fitted function with more significant fitting errors is enforced with a large value of ρ_n, while overfitting may result from a small ρ_n. To measure the out-of-sample performance of the fitted model, we consider the GCV criterion, as recommended in the literature (Mu et al., 2018; Wang and Wang, 2019; Wang et al., 2020b; Yu et al., 2020; Mu et al., 2020; Kim and Wang, 2021). Specifically, the roughness penalty parameter is chosen by minimizing the following expression over a grid of values of ρ_n: $\mathrm{GCV}(\rho_n) = \|\bar{\mathbf{Y}} - \mathbf{S}(\rho_n)\bar{\mathbf{Y}}\|^2/[N\{1 - \mathrm{tr}\{\mathbf{S}(\rho_n)\}/N\}^2]$, where $\mathbf{S}(\rho_n) = \mathbf{U}(\mathbf{U}^\top\mathbf{U} + n^{-1}\rho_n\mathbf{D})^{-1}\mathbf{U}^\top$ is the smoothing matrix.

4.4 Estimating the Quantile in SCCs

Since the quantile $q_{1-\alpha}$ used in Corollary 1 cannot be obtained analytically, we use a numerical simulation method to approximate it. First, we consider the bootstrap technique and simulate $\zeta_b(\boldsymbol{z})$ by $\widehat{G}_\eta^{-1/2}(\boldsymbol{z},\boldsymbol{z})\sum_{k=1}^{\kappa}\widehat{\lambda}_k^{1/2}Z_{k,b}\widehat{\psi}_k(\boldsymbol{z})$, where $\{Z_{k,b},\ k = 1,\ldots,\kappa,\ b = 1,\ldots,B\}$ are independent standard normal variables. Then, the quantile $q_{1-\alpha}$ can be estimated by the corresponding empirical quantile of these maximum values by taking the maximal absolute value for each copy of $\zeta_b(\boldsymbol{z})$.

For two-sample case, denote $\widehat{V}(\boldsymbol{z},\boldsymbol{z}') = \widehat{G}_{1\eta}(\boldsymbol{z},\boldsymbol{z}') + \tau\widehat{G}_{2\eta}(\boldsymbol{z},\boldsymbol{z}')$, then we simulate

$$\widehat{W}_b(\boldsymbol{z}) = \{\widehat{V}(\boldsymbol{z},\boldsymbol{z})\}^{-1/2}\left\{\sum_{k=1}^{\kappa_1}\widehat{\lambda}_{1k}^{1/2}Z_{1k,b}\widehat{\psi}_{1k}(\boldsymbol{z}) - (n_1/n_2)^{1/2}\sum_{k=1}^{\kappa_2}\widehat{\lambda}_{2k}^{1/2}Z_{2k,b}\widehat{\psi}_{2k}(\boldsymbol{z})\right\},\ \boldsymbol{z}\in\Omega.$$

Similarly, the quantile $q_{12,\alpha}$ can be estimated by the empirical quantile of level $1-\alpha$ of the B simulated $\|\widehat{W}_b\|_\infty$'s, $b = 1,\ldots,B$.

4.5 Adapting SCC to Account for Measurement Error

In this subsection, we propose a modification to the SCC procedure presented in Section 3 to handle objects that may not be feasible to satisfy Assumptions (A2) completely and (A3) regarding measurement errors.

In one-sample case, we first compute the estimate of $\sigma^2(\boldsymbol{z}_j)$, for any $j = 1, \ldots, N$, using $\widehat{\sigma}^2(\boldsymbol{z}_j) = n^{-1}\sum_{i=1}^{n}\widehat{\varepsilon}_{ij}\widehat{\varepsilon}_{ij}$, where $\widehat{\varepsilon}_{ij} = \widehat{R}_{ij} - \widehat{\eta}_i(\boldsymbol{z}_j)$, $\widehat{R}_{ij}$ is the residual for the ith object at the j-th voxel and $\widehat{\eta}_i(\boldsymbol{z})$ is the TPST estimator given in (3.1). Next, we denote $\widehat{\varepsilon}(\boldsymbol{z}) = \widetilde{\mathbf{B}}(\boldsymbol{z})^\top\boldsymbol{\Gamma}_{N,\rho}^{-1}\times\ n^{-1}N^{-1}\sum_{i=1}^{n}\sum_{j=1}^{N}\widetilde{\mathbf{B}}(\boldsymbol{z}_j)\sigma(\boldsymbol{z}_j)\varepsilon_{ij}$. We estimate the variance-covariance function of $\widehat{\varepsilon}(\boldsymbol{z})$, $\widetilde{G}_\varepsilon(\boldsymbol{z},\boldsymbol{z}') = \mathrm{Cov}\{\widehat{\varepsilon}(\boldsymbol{z}), \widehat{\varepsilon}(\boldsymbol{z}')\}$, by

$$\widehat{G}_\varepsilon(\boldsymbol{z},\boldsymbol{z}') = n^{-1}N^{-2}\widetilde{\mathbf{B}}(\boldsymbol{z})^\top\boldsymbol{\Gamma}_{N,\rho}^{-1}\left\{\sum_{j=1}^{N}\widetilde{\mathbf{B}}(\boldsymbol{z}_j)\widehat{\sigma}^2(\boldsymbol{z}_j)\widetilde{\mathbf{B}}(\boldsymbol{z}_j)^\top\right\}\boldsymbol{\Gamma}_{N,\rho}^{-1}\widetilde{\mathbf{B}}(\boldsymbol{z}'),$$

where $\boldsymbol{\Gamma}_{N,\rho}$ is given in (S2.9) in the Supplementary Material. We introduce a modified estimator $\widehat{\Sigma}(\boldsymbol{z},\boldsymbol{z}') = \widehat{G}_\eta(\boldsymbol{z},\boldsymbol{z}') + n\widehat{G}_\varepsilon(\boldsymbol{z},\boldsymbol{z}')$ and adjust the approximation procedure of quantile $q_{1-\alpha}$ as follows. First, we simulate

$$\zeta_b(\boldsymbol{z}) = \widehat{\Sigma}^{-1/2}(\boldsymbol{z},\boldsymbol{z})\left\{\sum_{k=1}^{\kappa}\widehat{\lambda}_k^{1/2}\widehat{\psi}_k(\boldsymbol{z})Z_{k,\xi}^{(b)} + \widetilde{\mathbf{B}}(\boldsymbol{z})^\top\boldsymbol{\Gamma}_{N,\rho}^{-1}\frac{1}{N}\sum_{j=1}^{N}\widetilde{\mathbf{B}}(\boldsymbol{z}_j)\widehat{\sigma}(\boldsymbol{z}_j)Z_{j,\varepsilon}^{(b)}\right\},$$

where $Z_{k,\xi}^{(b)}$ and $Z_{j,\varepsilon}^{(b)}$ are independent standard normal variables with $1 \le k \le \kappa, 1 \le j \le N$. Then, the $q_{1-\alpha}$ can be estimated by the corresponding empirical quantile of the B simulated values of $\|\zeta_b\|_\infty$. Finally, the SCC can be constructed as $\widehat{\mu}(\boldsymbol{z}) \pm n^{-1/2}q_{1-\alpha}\widehat{\Sigma}(\boldsymbol{z},\boldsymbol{z})^{1/2}$, $\boldsymbol{z} \in \Omega$.

For the two-sample case, we can modify the procedure similarly. First, for $H = 1, 2$, we define $\widehat{\sigma}_H(\boldsymbol{z})$ be the estimator of $\sigma_H(\boldsymbol{z})$, $\widehat{\Sigma}_H(\boldsymbol{z},\boldsymbol{z}') = \widehat{G}_{\eta,H} + n_H\widehat{G}_{\varepsilon,H}$, and $\widehat{\Xi}(\boldsymbol{z},\boldsymbol{z}') =$

$\widehat{\Sigma}_1(\boldsymbol{z},\boldsymbol{z}')+n_1/n_2\widehat{\Sigma}_2(\boldsymbol{z},\boldsymbol{z}')$. Then, to estimate $q_{12,\alpha}$, we simulate

$$\widehat{W}_b(\boldsymbol{z})=\left\{\widehat{\Xi}(\boldsymbol{z},\boldsymbol{z})\right\}^{-1/2}\left\{\sum_{k=1}^{\kappa_2}\widehat{\lambda}_{1k}^{1/2}Z_{1k,\xi}^{(b)}\widehat{\psi}_{1k}(\boldsymbol{z})-\left(\frac{n_1}{n_2}\right)^{1/2}\sum_{k=1}^{\kappa_2}\widehat{\lambda}_{2k}^{1/2}Z_{2k,\xi}^{(b)}\widehat{\psi}_{2k}(\boldsymbol{z})\right.$$
$$\left.+\widetilde{\mathbf{B}}(\boldsymbol{z})^\top\mathbf{\Gamma}_{N,\rho_1}^{-1}\frac{1}{N}\sum_{j=1}^{N}\widetilde{\mathbf{B}}(\boldsymbol{z}_j)\widehat{\sigma}_1(\boldsymbol{z}_j)Z_{1j,\varepsilon}^{(b)}-\left(\frac{n_1}{n_2}\right)^{1/2}\widetilde{\mathbf{B}}(\boldsymbol{z})^\top\mathbf{\Gamma}_{N,\rho_2}^{-1}\frac{1}{N}\sum_{j=1}^{N}\widetilde{\mathbf{B}}(\boldsymbol{z}_j)\widehat{\sigma}_2(\boldsymbol{z}_j)Z_{2j,\varepsilon}^{(b)}\right\},$$

where $Z_{Hk,\xi}^{(b)}$ and $Z_{Hj,\varepsilon}^{(b)}$ are independent standard normal variables with $1\le k\le\kappa_H, 1\le j\le N$ for $H=1,2$. Next, to estimate $q_{12,\alpha}$, we calculate the empirical quantile of the B simulated $\|\widehat{W}_b\|_\infty$, where $b=1,\ldots,B$. Finally, based on this estimate, we construct a modified SCC for $\mu_1(\boldsymbol{z})-\mu_2(\boldsymbol{z})$ as $(\widehat{\mu}_1-\widehat{\mu}_2)(\boldsymbol{z})\pm n_1^{-1/2}q_{12,\alpha}\{\widehat{\Xi}(\boldsymbol{z},\boldsymbol{z})\}^{1/2}$.

5. Simulation Studies

In this section, we conduct Monte Carlo simulations to evaluate the finite-sample performance of the proposed SCCs for the mean functions of complex 3D objects. To further demonstrate the superiority of the TPST estimators, a comparison with other competitors in the literature is provided in Section S1 of the Supplementary Material. The results highlight the superior performance of TPST, especially its ability to handle irregular domains.

The data are generated from the following model

$$Y_{ij}=\mu(\boldsymbol{z}_j)+\sum_{k=1}^{\kappa}\sqrt{\lambda_k}\xi_{ik}\psi_k(\boldsymbol{z}_j)+\sigma(\boldsymbol{z}_j)\varepsilon_{ij},\ \ \boldsymbol{z}_j=(z_{1j},z_{2j},z_{3j})\in\Omega, \tag{5.1}$$

for $i=1,\ldots,n$ and $j=1,\ldots,N$. We consider two irregularly shaped domains: a rectangle with a hole defined as $\Omega_1=\{\boldsymbol{z}\in[0,1]^3:\boldsymbol{z}_1\notin[1/3,2/3]$ or $\boldsymbol{z}_2\notin[1/3,2/3]\}$ and a ball-shaped domain defined as $\Omega_2=\{\boldsymbol{z}\in[0,1]^3:(z_1-0.5)^2+(z_2-0.5)^2+(z_3-0.5)^2\le 0.5^2\}$. Data are generated on these domains using model (5.1) by first creating data on M^3 equally spaced grid points in $[0,1]^3$, with M being 25 and 35, then

removing the points outside of Ω, resulting in N points. The sample size n is varied to evaluate the performance under both small and large sample sizes, with values of 50, 150, 300, and 600. To examine the performance under different scenarios, we choose the following mean functions: $\mu_1(\boldsymbol{z}) = 32\{(z_1 - 0.5)^2 + (z_2 - 0.5)^2 + (z_3 - 0.5)^2\}$; $\mu_2(\boldsymbol{z}) = 1.25(z_1 + z_2 + z_3)^3$; and $\mu_3(\boldsymbol{z}) = 4\exp\{(z_1 - 0.5)^2 + (z_2 - 0.5)^2 + (z_3 - 0.5)^2\}$.

The random noise ε_{ij} is i.i.d as $N(0,1)$ for $i = 1, \ldots, n$ and $j = 1, \ldots, N$ with $\sigma(\boldsymbol{z}) = 0.2\{1 - (z_1 - 0.5)^2 - (z_2 - 0.5)^2 - (z_3 - 0.5)^2\}$. To simulate the within-object dependence, we set $\xi_{ik} \overset{\text{i.i.d}}{\sim} N(0,1)$ for $i = 1, \ldots, n$ and $k = 1, \ldots, \kappa$, with $\kappa = 3$. The eigenvalues and eigenfunctions are $\lambda_1 = 0.5, \lambda_2 = 0.2, \lambda_3 = 0.1$ and $\psi_1(\boldsymbol{z}) = c_{11}\sin(\pi z_1) + c_{12}$, $\psi_2(\boldsymbol{z}) = c_2\cos(\pi z_2)$, $\psi_3(\boldsymbol{z}) = c_3(z_3 - 1/2)$. The constants c_{11}, c_{12}, c_2 and c_3 are chosen separately for different domains to ensure that $\int_{\Omega_i} \psi_k^2(\boldsymbol{z})\mathrm{d}\boldsymbol{z} = 1$ and $\int_{\Omega_i} \psi_k(\boldsymbol{z})\psi_{k'}(\boldsymbol{z})\mathrm{d}\boldsymbol{z} = 0$ for $i = 1, 2$, $k, k' = 1, \ldots, \kappa$ and $k' \neq k$. Specifically, $c_{11}^{(1)} = 1$, $c_{12}^{(1)} \approx 0.3674$, $c_2^{(1)} = 1.3342$ and $c_3^{(1)} = 3.3665$ when Ω_1 is considered, while $c_{11}^{(2)} = 1$, $c_{12}^{(2)} \approx 0.2240$, $c_2^{(2)} \approx 1.6154$ and $c_3^{(2)} \approx 4.1552$ for Ω_2.

5.1 Coverage Rate of One Sample SCC

The effectiveness of the TPST method proposed depends on d, r, and the choice of triangulations. In our simulations, we set smoothness of $r = 1$ and degrees $d = 4$, and use two different triangulations for each domain, $\triangle_1$ and $\triangle_2$. For the rectangle with a hole domain Ω_1, Figure 1 (a) and (b) show that there are 96 and 144 tetrahedra in $\triangle_{1,1}$ and $\triangle_{1,2}$, respectively. For the ball-shaped domain Ω_2, Figure 1 (c) and (d) show that there are 176 and 332 tetrahedra in $\triangle_{2,1}$ and $\triangle_{2,2}$, respectively.

We evaluate the reliability of the proposed one-sample SCCs of the mean functions by calculating the empirical coverage rate (ECR) for each replication. The ECR is

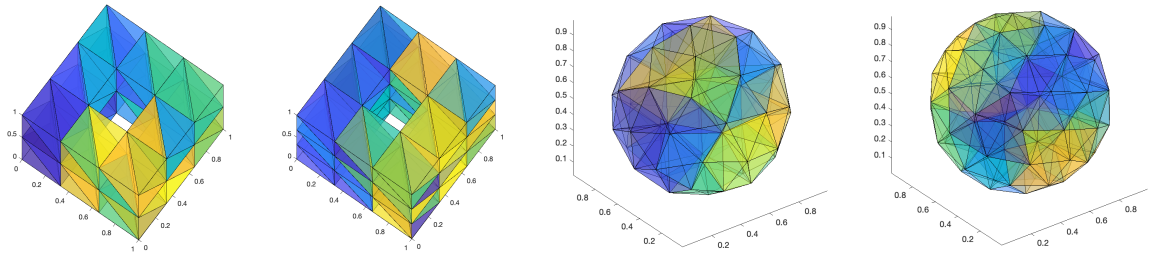

(a) $\triangle_{1,1}$ (b) $\triangle_{1,2}$ (c) $\triangle_{2,1}$ (d) $\triangle_{2,2}$

Figure 1: Triangulation of domain Ω_1 and Ω_2.

determined by testing if the true mean function is covered by the SCC at all grid points. Table 2 summarizes the results of 500 replications on the ball domain Ω_2 for the true mean functions μ_1, μ_2 and μ_3, with a nominal coverage level of $1-\alpha$, where α is set to 0.10, 0.05, and 0.01, respectively. The corresponding average width (AWD) of the SCC for each setting is also reported.

Table 2 reveals that as the sample sizes increase, the ECRs approach to the nominal confidence level and the AWDs decrease. These findings support our conclusion in Corollary 1. The majority of the cases show that the ECRs reach the nominal coverage level at around $n = 150 \sim 300$ regardless of the settings. Additionally, we observe that the choice of triangulation has minimal impact on the performance of the SCC, demonstrating the robustness of the proposed method. Our results in Section S1 of the Supplementary Materials also show that the estimation performance of TPST is not significantly impacted as long as the triangulation is sufficiently fine and properly constructed.

5.2 Power of hypothesis test based on Two Sample SCC

The SCC can also be used to calculate P-values in hypothesis testing. For example, when comparing the means of two independent populations, the P-value calculated

Table 1: Empirical coverage rates (ECRs) in percentage and corresponding average widths (AWDs) of the SCCs for mean functions μ_1, μ_2, and μ_3 over domain Ω_1. The AWDs are shown in parentheses.

Sample	Number of Grid Points (M^3)											
	$25 \times 25 \times 25$						$35 \times 35 \times 35$					
Size	$\alpha = .10$		$\alpha = .05$		$\alpha = .01$		$\alpha = .10$		$\alpha = .05$		$\alpha = .01$	
n	$\triangle_{1,1}$	$\triangle_{1,2}$	$\triangle_{1,1}$	$\triangle_{1,2}$	$\triangle_{1,1}$	$\triangle_{1,2}$	$\triangle_{1,1}$	$\triangle_{1,2}$	$\triangle_{1,1}$	$\triangle_{1,2}$	$\triangle_{1,1}$	$\triangle_{1,2}$
Mean Function: μ_1												
50	85.2	85.4	91.4	91.2	98.0	97.4	85.4	85.4	91.8	91.2	97.8	97.4
	(.614)	(.617)	(.684)	(.688)	(.821)	(.825)	(.608)	(.610)	(.678)	(.681)	(.815)	(.818)
150	90.2	90.0	94.6	94.8	98.2	98.4	90.4	90.0	94.6	94.6	98.2	98.4
	(.360)	(.362)	(.400)	(.403)	(.481)	(.483)	(.356)	(.358)	(.397)	(.399)	(.478)	(.479)
300	90.8	91.0	94.4	94.2	98.8	98.8	90.8	90.8	94.2	94.2	98.8	98.8
	(.255)	(.257)	(.284)	(.286)	(.341)	(.343)	(.252)	(.254)	(.281)	(.283)	(.339)	(.340)
600	89.8	90.0	94.6	94.6	99.4	99.4	90.0	89.8	94.8	94.8	99.4	99.4
	(.180)	(.182)	(.201)	(.202)	(.241)	(.243)	(.179)	(.179)	(.199)	(.200)	(.240)	(.241)
Mean Function: μ_2												
50	85.2	85.2	91.2	91.4	97.6	97.4	85.2	85.4	91.6	91.0	97.6	97.4
	(.610)	(.613)	(.681)	(.683)	(.818)	(.821)	(.606)	(.608)	(.677)	(.678)	(.814)	(.816)
150	90.0	88.2	94.2	94.2	98.0	98.2	90.2	89.8	94.6	94.6	98.2	98.4
	(.358)	(.358)	(.399)	(.399)	(.480)	(.480)	(.355)	(.356)	(.396)	(.397)	(.477)	(.478)
300	90.8	90.8	94.4	94.2	98.8	98.8	90.8	90.6	94.4	94.4	98.8	98.8
	(.255)	(.256)	(.284)	(.285)	(.341)	(.343)	(.252)	(.253)	(.281)	(.282)	(.339)	(.340)
600	89.8	89.8	94.6	94.6	99.4	99.4	89.6	89.6	94.8	94.8	99.4	99.4
	(.180)	(.181)	(.201)	(.202)	(.241)	(.242)	(.178)	(.179)	(.199)	(.200)	(.239)	(.240)
Mean Function: μ_3												
50	85.2	85.4	91.2	91.4	97.8	97.4	85.4	85.4	91.2	90.8	97.6	97.4
	(.610)	(.613)	(.681)	(.683)	(.818)	(.821)	(.606)	(.608)	(.677)	(.678)	(.814)	(.816)
150	90.2	89.6	94.6	94.8	98.2	98.2	90.4	90.2	94.6	94.6	98.2	98.4
	(.359)	(.361)	(.400)	(.402)	(.480)	(.482)	(.355)	(.357)	(.396)	(.398)	(.477)	(.479)
300	90.8	91.0	94.4	94.2	98.8	98.8	90.8	90.6	94.4	94.4	98.8	98.8
	(.255)	(.256)	(.284)	(.285)	(.341)	(.343)	(.252)	(.253)	(.281)	(.282)	(.339)	(.340)
600	89.6	89.8	94.6	94.6	99.4	99.4	89.6	89.6	94.6	94.8	99.4	99.4
	(.180)	(.181)	(.201)	(.202)	(.241)	(.242)	(.178)	(.179)	(.199)	(.200)	(.239)	(.240)

using the two-sample SCC provides an indication of the strength of evidence against the null hypothesis of equal means. In this study, we evaluate the power of the two-sample test based on the two-sample SCC by conducting the hypothesis test for the difference of the following two independent population means:

$$H_0: \ \mu_1(\boldsymbol{z}) = \mu_2(\boldsymbol{z}), \text{ for all } \boldsymbol{z} \in \Omega_2 \quad \text{v.s.} \quad H_a: \ \mu_1(\boldsymbol{z}) \neq \mu_2(\boldsymbol{z}) \text{ for some } \boldsymbol{z} \in \Omega_2.$$

As with the data generation process outlined in Section 5.1, two groups of data are

Table 2: Empirical coverage rates (ECRs) in percentage and corresponding average widths (AWDs) of the SCCs for mean functions μ_1, μ_2, and μ_3 over domain Ω_2. The AWDs are shown in parentheses.

Sample	Number of Grid Points (M^3)											
	$25 \times 25 \times 25$						$35 \times 35 \times 35$					
Size	$\alpha = .10$		$\alpha = .05$		$\alpha = .01$		$\alpha = .10$		$\alpha = .05$		$\alpha = .01$	
n	$\triangle_{2,1}$	$\triangle_{2,2}$	$\triangle_{2,1}$	$\triangle_{2,2}$	$\triangle_{2,1}$	$\triangle_{2,2}$	$\triangle_{2,1}$	$\triangle_{2,2}$	$\triangle_{2,1}$	$\triangle_{2,2}$	$\triangle_{2,1}$	$\triangle_{2,2}$
Mean Function: μ_1												
50	86.2	85.6	91.8	92.0	98.2	97.6	86.0	86.4	91.2	91.4	98.0	98.0
	(.609)	(.612)	(.678)	(.682)	(.812)	(.816)	(.595)	(.599)	(.665)	(.668)	(.801)	(.805)
150	90.0	89.6	93.8	94.6	98.2	98.0	90.2	89.8	94.8	94.6	98.0	97.4
	(.356)	(.358)	(.396)	(.398)	(.476)	(.478)	(.348)	(.350)	(.389)	(.391)	(.468)	(.470)
300	91.2	91.4	94.0	94.2	99.0	99.0	91.6	91.2	94.4	94.8	99.0	99.0
	(.252)	(.254)	(.281)	(.282)	(.338)	(.339)	(.247)	(.248)	(.275)	(.277)	(.333)	(.334)
600	89.8	89.6	95.0	94.8	99.2	99.0	90.4	90.4	96.0	96.2	99.4	99.4
	(.178)	(.180)	(.199)	(.200)	(.239)	(.240)	(.175)	(.176)	(.195)	(.196)	(.235)	(.236)
Mean Function: μ_2												
50	86.2	85.8	91.8	91.4	98.2	97.8	86.0	86.4	91.0	91.4	98.0	98.0
	(.606)	(.608)	(.675)	(.677)	(.810)	(.812)	(.594)	(.598)	(.664)	(.667)	(.800)	(.804)
150	89.6	89.6	94.0	94.2	98.0	98.0	90.4	89.8	94.8	94.8	97.8	97.6
	(.354)	(.356)	(.394)	(.396)	(.474)	(.476)	(.347)	(.349)	(.388)	(.390)	(.468)	(.470)
300	91.0	91.6	94.0	94.2	99.0	99.0	91.6	91.2	94.4	94.8	99.0	99.0
	(.252)	(.254)	(.281)	(.282)	(.337)	(.339)	(.247)	(.248)	(.275)	(.277)	(.333)	(.334)
600	89.8	89.6	95.0	94.8	99.2	99.0	90.4	90.6	96.0	96.2	99.4	99.4
	(.178)	(.180)	(.199)	(.200)	(.239)	(.240)	(.175)	(.176)	(.195)	(.196)	(.235)	(.236)
Mean Function: μ_3												
50	86.2	85.8	91.8	91.4	98.2	97.8	86.0	86.4	91.0	91.4	98.0	98.0
	(.606)	(.608)	(.675)	(.678)	(.810)	(.812)	(.594)	(.598)	(.664)	(.667)	(.800)	(.804)
150	90.0	89.8	93.8	94.2	98.0	98.0	90.4	89.6	94.8	94.8	97.8	97.6
	(.354)	(.356)	(.394)	(.396)	(.474)	(.476)	(.347)	(.349)	(.388)	(.390)	(.468)	(.470)
300	91.0	91.6	94.0	94.2	99.0	99.0	91.6	91.2	94.6	94.8	99.0	99.0
	(.252)	(.254)	(.281)	(.282)	(.337)	(.339)	(.247)	(.248)	(.275)	(.277)	(.333)	(.334)
600	89.8	89.8	95.2	94.8	99.2	99.0	90.4	90.6	96.0	96.2	99.4	99.4
	(.178)	(.180)	(.199)	(.200)	(.239)	(.240)	(.175)	(.176)	(.195)	(.196)	(.235)	(.236)

generated in the ball domain Ω_2 with $35 \times 35 \times 35$ grid points using the model

$$Y_{H,ij} = \mu_H(\boldsymbol{z}_j) + \sum_{k=1}^{\kappa} \sqrt{\lambda_k}\xi_{ij}\psi_k(\boldsymbol{z}_j) + \sigma(\boldsymbol{z}_j)\varepsilon_{ij}, \ H = 1, 2,$$

where with abusing of notations, $\mu_1(\boldsymbol{z}) = 32\{(z_1 - 0.5)^2 + (z_2 - 0.5)^2 + (z_3 - 0.5)^2\}$, $\mu_2(\boldsymbol{z}) = \mu_1(\boldsymbol{z}) + \delta(z_1 + z_2 + z_3)^3$ and $\sigma(\boldsymbol{z}) = 0.15$. The parameter δ measures the discrepancy between mean functions μ_1 and μ_2; thus, larger values δ shift the second

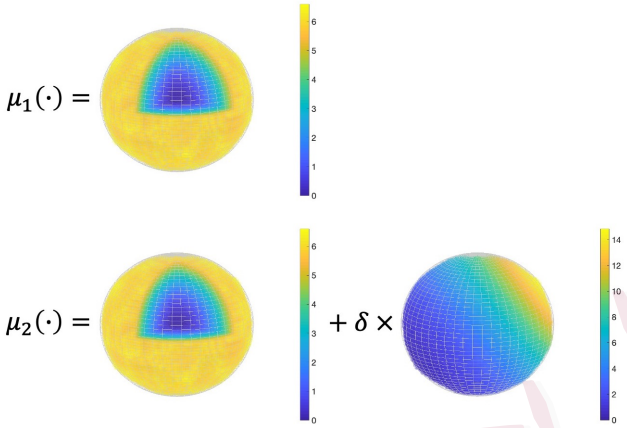

Figure 2: Design of μ_1 and μ_2 in the simulation study of two-sample SCC.

group data further away from the first, therefore more in favor of H_a. The design of the two sample mean functions within the domain Ω_2 is depicted in Figure 2. In this simulation experiment, we select δ from 0, 0.005 and another 10 grid points evenly spaced from 0.01 to 0.1.

We reject H_0 if the constant function of zero is not covered entirely by the SCC constructed for the $\mu_2 - \mu_1$. Figure 3 displays the rejection rates out of 500 iterations as δ varies, for significance level $\alpha = 0.10$, 0.05 and 0.01, respectively. At $\delta = 0$, the rejection rate represents the empirical probability of Type I error, while for $\delta > 0$, the rejection rate corresponds to the empirical power. We can tell from Figure 3 that our method provides an efficient and powerful tool for two-sample inference. At $\delta = 0$, the rejection rates are close to or equal to the significance level α. As the sample size n and discrepancy parameter δ increase, the empirical power increases rapidly to reach a maximum of 1. As the significance level α decreases, the empirical power increases more quickly. Even with a moderately small sample size $n = 150$ and a significance level of $\alpha = 0.05$, the proposed method can detect slight differences between two groups of data. This highlights the robustness of the method, even with small sample sizes

and stringent significance levels.

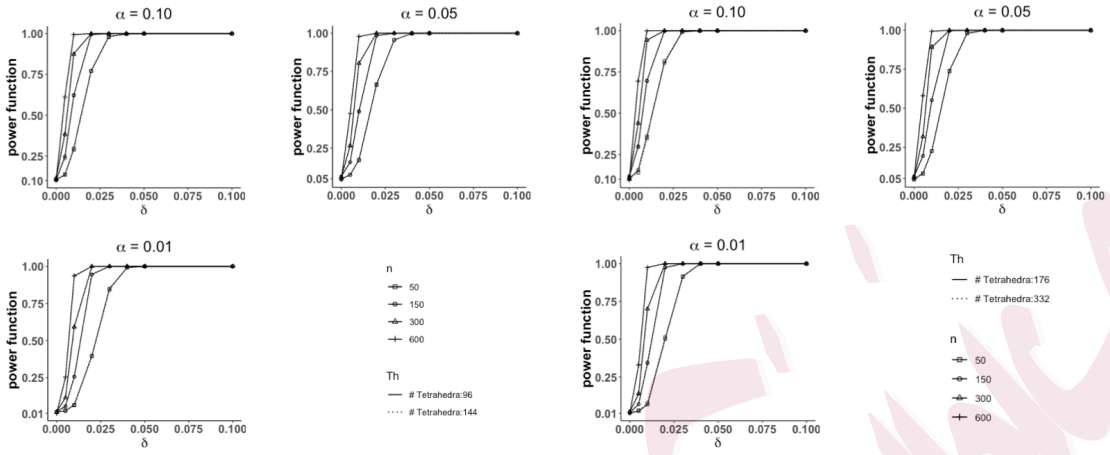

(a) Ω_1 (b) Ω_2

Figure 3: Empirical type I error and power of two-Sample test for different significance levels (α) in simulation studies on Ω_1 and Ω_2 domains.

6. Real Data Analysis

Today's medical studies rely heavily on large imaging data to gain insights into diseases like Alzheimer's disease (AD), which is the most common cause of dementia in the aging population. Despite its high prevalence, there is currently no cure or specific treatment to halt its progression. Early diagnosis of AD is crucial as new drug therapies may potentially slow down its progression, as per recent studies (Leifer, 2003). FDG-PET is a widely available in vivo method of investigating brain metabolism regionally (Ishii, 2014), and it has become one of the most promising tools for the early diagnosis of AD (Brown et al., 2014). In this section, we implement the proposed procedures to locate the significant effect of AD and understand the association between PET images and cognitive impairment.

The data for this study was obtained from the Alzheimer's Disease Neuroimag-

ing Initiative (ADNI) study, which can be found at `http://adni.loni.usc.edu`. In ADNI1 and ADNI GO studies, a total of 447 FDG-PET scans were acquired from participants aged between 55 to 90 years, including 112 cognitively normal (CON) subjects, 213 subjects with mild cognitive impairment (MCI), and 122 subjects diagnosed with Alzheimer's disease (AD). Figure 4 illustrates examples of slices of the PET images and the triangulations used to analyze the scans.

In this study, the TPST method is applied with a smooth parameter of $r = 1$ and a degree of $d = 8$ for both mean and covariance function estimation. The proposed two-sample SCC procedure is then implemented by grouping the subjects based on their diagnosis results. Figure 4 (c) reports the significant regions identified by comparing neural FDG-PET scans between AD and CON groups. As shown, there is less glucose uptake in classic default mode network areas (d-f) as expected, in AD patients compared to CON participants. These areas are most active "at rest" and are thought to be critical for integrating attention, autobiographical memory, and associated memory traces. Learning and memory, as well as recognition areas, are also seen for a large region extending from inferior to medial temporal cortices (a-b) in Figure 4 (c). While atrophy in these areas is a quintessential MR biomarker for AD onset and progression, hypometabolism is seen in this region for patients showing pronounced memory decline. Finally, the head to the main body of the caudate (c) in Figure 4 (c) was seen. While this is a classic if often ignored finding, the extent here is larger and more posterior. Curiously, by contrast, more uptake was seen in pre- and post-central gyri (1), the thalamus (2), and most of the hindbrain, including the brainstem and cerebellum. These are basic sensory processing areas, including the "what" and "where" visual pathways, somatosensory pathways, and the primary motor cortex for initiating movement. These

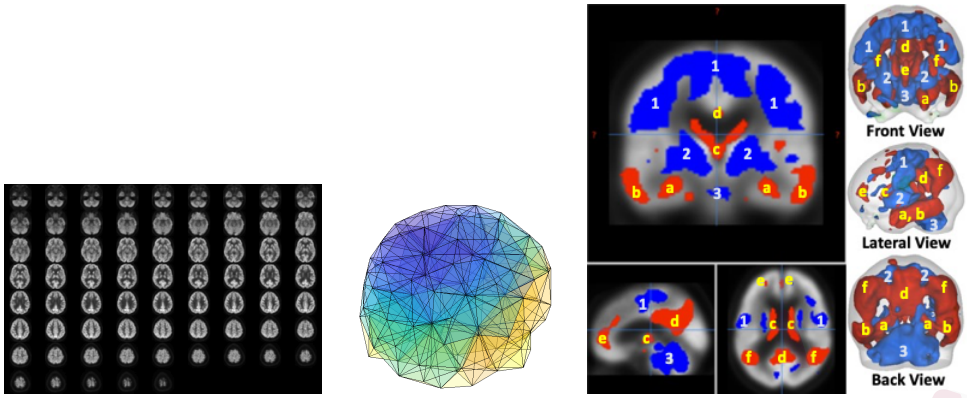

(a) Example of PET Image (b) Triangulation (c) Significant regions

Figure 4: (a) An example of a PET image; (b) the triangulated domain of a human brain; and (c) visual representation of significant regions in the comparison between subjects in the CON and AD groups, based on the coverage of zero by the SCC. The regions marked in red indicate areas where zero exceeds the upper SCC threshold, while regions in blue indicate areas where zero falls below the lower SCC threshold.

results may support the Sensory Deficit Theory, which suggests that decline in sensory processing leads to cognitive decline. Similar findings have been discussed in existing works, such as Mullins et al. (2018); Halawa and Marshall (2018); Yassine et al. (2022). These works suggest that our proposed statistical inference procedure for analyzing complex 3D objects may contribute to the understanding of factors associated with Alzheimer's Disease (AD) and aid in the detection of AD development.

7. Conclusions and Discussion

The challenge of analyzing complex objects such as 3D imaging in medical research has long been a difficult problem due to the complexities in developing statistical methods that effectively handle irregularly shaped data. In this study, we proposed a statistical inference procedure that overcomes these difficulties and provides a powerful tool for identifying specific regions within the object where the signal is strong or where differences exist between different groups of subjects.

The contributions of this article are significant in several ways. From a scientific perspective, our proposed method provides a general procedure and systematic solution for complex object/image analysis problems, specifically the localization of significant regions. From a mathematical analytics viewpoint, our approach is efficient and systematic, addressing the complex 3D object analysis with irregular domains, unlike existing methods that are restricted to regular boundaries and require large memory and computation power. From a statistical methodology perspective, our proposed method provides a general statistical framework for functional regression models with complex object responses, which can be used to develop many models and extensions, such as function on scalar regression. Lastly, fusing images of the same target acquired with varying resolutions from multiple sensors or study groups is a crucial issue in the field of image fusion. Our proposed estimation and inference framework enables seamless extension of the SCC to accommodate objects collected with diverse resolutions.

Given the positive outcomes of this study, there are various avenues for future research. One area of investigation could be focused on overcoming the challenges posed by the enormous size of complex 3D object data. With the increasing availability of high-resolution imaging technology, the size of complex object datasets continues to grow, making them difficult to handle and analyze efficiently. A potential solution is to investigate parallel computing techniques, such as distributed computing, to speed up the analysis process. It is essential, however, to thoroughly evaluate the theoretical guarantees of these methods before implementation. This presents a valuable area for future study and exploration.

Finally, it would be worthwhile to extend the procedure to a larger and more diverse dataset to determine its ability to generalize across different populations. Through on-

going improvement and refinement of techniques for analyzing complex medical imaging data, we can continue to expand our understanding of the underlying mechanisms of diseases like Alzheimer's and improve treatments for these debilitating conditions.

Acknowledgement

Li Wang's research was partially supported by the National Science Foundation grant DMS-2203207. Guannan Wang's research was supported in part by Simons Foundation Mathematics and Physical Sciences-Collaboration Grant for Mathematicians #963447. Data used in preparation of this article were obtained from the Alzheimer's Disease Neuroimaging Initiative (ADNI) database (`ADNI.loni.usc.edu`). The investigators within the ADNI contributed to the design and implementation of ADNI and/or provided data but did not participate in analysis or writing of this report. A complete listing of ADNI investigators can be found at `http://adni.loni.usc.edu/wp-content/uploads/how_to_apply/ADNI_Acknowledgement_List.pdf`.

Supplementary Material

In the Supplementary Material, we provide additional simulation studies and detailed proofs of the theoretical results in this article.

References

Bowman, F. D., Caffo, B., Bassett, S. S., and Kilts, C. (2008), "A Bayesian hierarchical framework for spatial modeling of fMRI data," *NeuroImage*, 39, 146–156.

Brown, R. K., Bohnen, N. I., Wong, K. K., Minoshima, S., and Frey, K. A. (2014), "Brain PET in suspected dementia: patterns of altered FDG metabolism," *Radiographics*, 34, 684–701.

Cao, G., Wang, J., Wang, L., and Todem, D. (2012a), "Spline confidence bands for functional derivatives," *Journal of Statistical Planning and Inference*, 142, 1557–1570.

Cao, G. and Wang, L. (2018), "Simultaneous inference for the mean of repeated functional data," *Journal of Multivariate Analysis*, 165, 279–295.

Cao, G., Yang, L., and Todem, D. (2012b), "Simultaneous inference for the mean function based on dense functional data," *Journal of nonparametric statistics*, 24, 359–377.

Chang, C., Lin, X., and Ogden, R. T. (2017), "Simultaneous confidence bands for functional regression models," *Journal of Statistical Planning and Inference*, 188, 67–81.

Choi, H. and Reimherr, M. (2018), "A geometric approach to confidence regions and bands for functional parameters," *Journal of the Royal Statistical Society: Series B (Statistical Methodology)*, 80, 239–260.

Dai, X., Müller, H.-G., et al. (2018), "Principal component analysis for functional data on riemannian manifolds and spheres," *The Annals of Statistics*, 46, 3334–3361.

Degras, D. A. (2011), "Simultaneous confidence bands for nonparametric regression with functional data," *Statistica Sinica*, 21, 1735–1765.

Dubey, P. and Müller, H.-G. (2019), "Fréchet analysis of variance for random objects," *Biometrika*, 106, 803–821.

Goldsmith, J., Greven, S., and Crainiceanu, C. (2013), "Corrected confidence bands for functional data using principal components," *Biometrics*, 69, 41–51.

Gu, L., Wang, L., Härdle, W. K., and Yang, L. (2014), "A simultaneous confidence corridor for varying coefficient regression with sparse functional data," *Test*, 23, 806–843.

Halawa, O. A. and Marshall, G. A. (2018), "Inferior and medial temporal tau and cortical amyloid are associated with daily functional impairment in Alzheimer's disease," *Alzheimer's & Dementia*, 14, 1275–1276.

Hall, P., Müller, H.-G., and Wang, J.-L. (2006), "Properties of principal component methods for functional and longitudinal data analysis," *The Annals of Statistics*, 34, 1493–1517.

Ishii, K. (2014), "PET approaches for diagnosis of dementia," *American Journal of Neuroradiology*, 35, 2030–2038.

Kim, M. and Wang, L. (2021), "Generalized spatially varying coefficient models," *Journal of Computational and Graphical Statistics*, 30, 1–10.

Lai, M. J. and Schumaker, L. L. (2007), *Spline functions on triangulations.*, Cambridge University Press.

Lai, M. J. and Wang, L. (2013), "Bivariate penalized splines for regression." *Statistica Sinica*, 23, 1399–1417.

Lazar, N. A. (2008), *The statistical analysis of functional MRI data*, vol. 7, Springer.

Leifer, B. P. (2003), "Early diagnosis of Alzheimer's disease: clinical and economic benefits," *Journal of the American Geriatrics Society*, 51, S281 – S288.

Li, L. and Zhang, X. (2017), "Parsimonious tensor response regression," *Journal of the American Statistical Association*, 112, 1131–1146.

Li, X., Wang, L., and Wang, H. J. (2021), "Sparse learning and structure identification for ultrahigh-dimensional image-on-scalar regression," *Journal of the American Statistical Association*, 116, 1994–2008.

Li, X., Yu, S., Wang, Y., Wang, G., and Wang, L. (2022), "Nonparametric regression for 3D point cloud Learning," *arXiv preprint arXiv:2106.04255*.

Li, Y., Wang, N., and Carroll, R. J. (2013), "Selecting the number of principal components in functional data," *Journal of the American Statistical Association*, 108, 1284–1294.

Morris, J. S. and Carroll, R. J. (2006), "Wavelet-based functional mixed models," *Journal of the Royal Statistical Society: Series B (Statistical Methodology)*, 68, 179–199.

Mu, J., Wang, G., and Wang, L. (2018), "Estimation and inference in spatially varying coefficient models," *Environmetrics*, 29, e2485.

— (2020), "Spatial autoregressive partially linear varying coefficient models," *Journal of Nonparametric Statistics*, 32, 428–451.

Mullins, R., Reiter, D., and Kapogiannis, D. (2018), "Magnetic resonance spectroscopy reveals abnormalities of glucose metabolism in the Alzheimer's brain," *Annals of Clinical and Translational Neurology*, 5, 262–272.

Nathoo, F. S., Kong, L., Zhu, H., and Initiative, A. D. N. (2019), "A review of statistical methods in imaging genetics," *Canadian Journal of Statistics*, 47, 108–131.

Persson, P.-O. and Strang, G. (2004), "A simple mesh generator in MATLAB," *SIAM Review*, 46, 329–345.

Petersen, A., Müller, H.-G., et al. (2019), "Fréchet regression for random objects with Euclidean predictors," *The Annals of Statistics*, 47, 691–719.

Project, T. C. (2020), *CGAL user and reference manual*, CGAL Editorial Board, 5th ed.

Ramsay, J. and Silverman, B. (2005), *Functional Data Analysis*, Springer.

Scouten, A., Papademetris, X., and Constable, R. T. (2006), "Spatial resolution, signal-to-noise ratio, and smoothing in multi-subject functional MRI studies," *Neuroimage*, 30, 787–793.

Si, H. (2015), "TetGen, a Delaunay-based quality tetrahedral mesh generator," *ACM Transactions on Mathematical Software (TOMS)*, 41, 1–36.

Wang, G. and Wang, J. (2019), "On selection of semiparametric spatial regression models," *Stat*, 8, e221.

Wang, J., Cao, G., Wang, L., and Yang, L. (2020a), "Simultaneous confidence band for stationary covariance function of dense functional data," *Journal of Multivariate Analysis*, 176, 104584.

Wang, J.-L., Chiou, J.-M., and Müller, H.-G. (2016), "Review of functional data analysis," *Annual Review of Statistics and Its Application*, 3, 257–295.

Wang, L., Wang, G., Lai, M.-J., and Gao, L. (2020b), "Efficient estimation of partially linear models for data on complicated domains by bivariate penalized splines over triangulations," *Statistica Sinica*, 30, 347–369.

Wang, Y., Wang, G., Wang, L., and Ogden, R. T. (2020c), "Simultaneous confidence corridors for mean functions in functional data analysis of imaging data," *Biometrics*, 76, 427–437.

Yao, F., Müller, H.-G., and Wang, J.-L. (2005), "Functional data analysis for sparse longitudinal data," *Journal of the American Statistical Association*, 100, 577–590.

Yassine, H. N., Solomon, V., Thakral, A., Sheikh-Bahaei, N., Chui, H. C., Braskie, M. N., Schneider, L. S., and Talbot, K. (2022), "Brain energy failure in dementia syndromes: opportunities and challenges for glucagon-like peptide-1 receptor agonists," *Alzheimer's & Dementia*, 18, 478–497.

Yu, S., Wang, G., Wang, L., Liu, C., and Yang, L. (2020), "Estimation and inference for generalized geoadditive models," *Journal of the American Statistical Association*, 115, 761–774.

Yu, S., Wang, G., Wang, L., and Yang, L. (2021), "Multivariate spline estimation and inference for image-on-scalar regression," *Statistica Sinica*, 31, 1463–1487.

Zhu, H., Fan, J., and Kong, L. (2014), "Spatially varying coefficient model for neuroimaging data with jump discontinuities," *Journal of the American Statistical Association*, 109, 1084–1098.

Zhu, H., Li, R., and Kong, L. (2012), "Multivariate varying coefficient model for functional responses," *The Annals of statistics*, 40, 2634–2666.

Zhu, H., Li, T., and Zhao, B. (2022), "Statistical learning methods for neuroimaging data analysis with applications," *arXiv preprint arXiv:2210.09217*.

Yueying Wang

Amazon.com, Inc.,

Bellevue, WA 98170

E-mail: (yueyingw@amazon.com)

Guannan Wang

Department of Mathematics, William & Mary,

Williamsburg, VA 23185

E-mail: (gwang01@wm.edu)

Brandon Klinedinst

Department of Medicine, University of Washington,

Seattle, WA 98195

E-mail: (brandon.klinedinst@gmail.com)

Auriel Willette

Department of Food Science and Human Nutrition, Iowa State University,

Ames, IA 50011

E-mail: (awillett@iastate.edu)

Li Wang

Department of Statistics, George Mason University,

Fairfax, VA 22030

E-mail: (lwang41@gmu.edu)